Mesoscopic Klein-Schwinger effect in graphene

A. Schmitt, P. Vallet, D. Mele, M. Rosticher, T. Taniguchi, K. Watanabe, E. Bocquillon, G. Fève, Jean-Marc Berroir, C. Voisin, et al.

nature physics

Article

https://doi.org/10.1038/s41567-023-01978-9

Mesoscopic Klein-Schwinger effect in graphene

Received: 26 July 2022

Accepted: 1 February 2023

Published online: 09 March 2023

Check for updates

A. Schmitt[1] ✉, P. Vallet[2], D. Mele[1,3], M. Rosticher[1], T. Taniguchi[4], K. Watanabe[4], E. Bocquillon[1,5], G. Fève[1], J. M. Berroir[1], C. Voisin[1], J. Cayssol[1,2], M. O. Goerbig[6], J. Troost[1], E. Baudin[1] ✉ & B. Plaçais[1] ✉

Strong electric field annihilation by particle–antiparticle pair creation, also known as the Schwinger effect, is a non-perturbative prediction of quantum electrodynamics. Its experimental demonstration remains elusive, as threshold electric fields are extremely strong and beyond current reach. Here, we propose a mesoscopic variant of the Schwinger effect in graphene, which hosts Dirac fermions with an approximate electron–hole symmetry. Using transport measurements, we report on universal one-dimensional Schwinger conductance at the pinchoff of ballistic graphene transistors. Strong pinchoff electric fields are concentrated within approximately 1 μm of the transistor's drain and induce Schwinger electron–hole pair creation at saturation. This effect precedes a collective instability towards an ohmic Zener regime, which is rejected at twice the pinchoff voltage in long devices. These observations advance our understanding of current saturation limits in ballistic graphene and provide a direction for further quantum electrodynamic experiments in the laboratory.

A variety of important physical phenomena require a non-perturbative understanding of quantum field theory. This includes solitonic waves, but also several deeply quantum mechanical phenomena like the confinement of quarks in quantum chromodynamics. While many non-perturbative problems are notably hard to compute, some are within reach and yield accurate predictions. Among the most striking non-perturbative predictions of quantum field theory is the instability of an electric field under the creation of particle–antiparticle pairs. The Schwinger effect (SE) states that pairs are created, out of a false vacuum with an electric field, to minimize energy. It is a simple yet non-trivial and non-perturbative prediction of quantum electrodynamics[1–4]. The pair-creation rate w per unit d-dimensional volume writes as the n-th order perturbation development $w(E) \propto \sum_{n\geq 1}\left(\frac{E}{n}\right)^{\frac{d+1}{2}} e^{-\pi\frac{nE_S}{E}}$ (see prefactors in ref. [4] and Supplementary Discussion Section I), where E is the electric field and $E_S = \Delta_S^2/e\hbar c = 1.32\,10^{18}\ \mathrm{Vm}^{-1}$ (with e the elementary charge, c the speed of light and $\hbar$ the reduced Planck constant), called the Schwinger field, corresponds to the electron-mass energy $\Delta_S = mc^2 = 511$ keV, $2\Delta_S$ being the threshold energy needed to create an electron–positron pair at a characteristic length-scale given by the Compton length $\lambda_C = \hbar c/\Delta_S$. Large efforts have been devoted to produce such extremely strong electric fields in the laboratory to check this prediction explicitly[5]. Unfortunately, the attempts to observe the SE in the last decades have not yet met with success.

With the advent of graphene, a novel playground for the study of relativistic effects has been opened in the completely different framework of condensed matter physics[6–11]. In such a mesoscopic variant, electron–positron pairs are substituted by electron–hole pairs, speed of light c by the Fermi velocity $v_F \simeq 10^6\ \mathrm{m\,s}^{-1}$, and the rest energy by a bandgap (Interpretation of the Schwinger voltage). While graphene is intrinsically gapless, we show below that an effective gap is provided for one-dimensional (1D) transport. Our experiments point out that

[1]Laboratoire de Physique de l'Ecole normale supérieure, ENS, Université PSL, CNRS, Sorbonne Université, Université Paris-Cité, Paris, France. [2]Laboratoire Ondes et Matière d'Aquitaine, Talence, France. [3]Université de Lille, CNRS, Centrale Lille, Université Polytechnique Hauts-de-France, Junia-ISEN, UMR 8520-IEMN, Lille, France. [4]Advanced Materials Laboratory, National Institute for Materials Science, Tsukuba, Japan. [5]II. Physikalisches Institut, Universität zu Köln, Köln, Germany. [6]Laboratoire de Physique des Solides, CNRS UMR 8502, Univ. Paris-Sud, Université Paris-Saclay, Orsay Cedex, France. ✉e-mail: aurelien.schmitt@phys.ens.fr; emmanuel.baudin@phys.ens.fr; bernard.placais@phys.ens.fr

https://doi.org/10.1038/s41567-023-01978-9

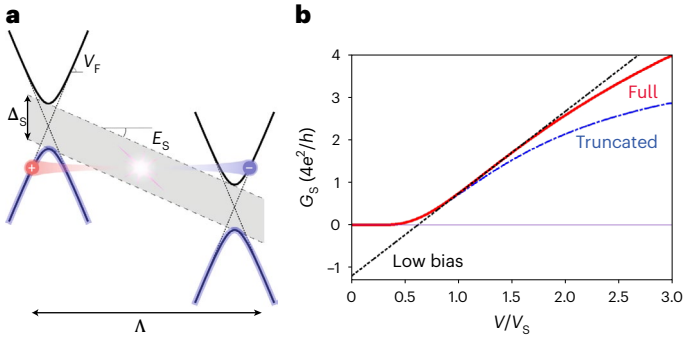

Fig. 1 | Mesoscopic SE for massive 1D Dirac fermions. a, Sketch of the 1D SE across a graphene junction of length Λ and gap Δ_S, defining a Schwinger field $E_S = \Delta_S^2/e\hbar v_F$ and a junction Schwinger voltage $V_S = E_S\Lambda$. It leads to the proliferation of electron–hole pairs at a rate $w_{1d}\Lambda$, with w_{1d} given by equation (1) and a pair current given by equation (2). **b**, The differential conductance $G_S = \partial I_S/\partial V$ given by equation (3) for $g_s = g_v = 2$ (red line). It is well approximated by the affine approximation (equation 4), $G_S = 1.20\left(\frac{V}{V_C} - 1\right) \times \frac{4e^2}{h}$, with $V_C = 0.62\ V_S$ (black dashed line). The truncated (first-order perturbation) Schwinger conductance (blue dash-dotted line), $G_S^* = 4g_sg_v\frac{e^2}{h}\left(1 + \pi\frac{V_S}{V}\right)e^{-\pi\frac{V_S}{V}}$ (main text), substantially deviates from the full series (equation 3).

this effective energy scale Δ_S is less than 0.2 eV, in which case the Schwinger fields $E_S = \Delta_S^2/e\hbar v_F \lesssim 6.10^7\ \mathrm{Vm}^{-1}$ are experimentally accessible, while remaining smaller than breakdown fields of the embedding hexagonal boron nitride (hBN) dielectric[12]. Neutral single-layer graphene, considered in refs. [8–10], corresponds to the gapless two-dimensional (2D) limit where $E_S = 0$ so that the 2D Schwinger rate reduces to a superlinear $J \propto E^{\frac{3}{2}}$ current density–field relation. This power law is indeed observed in single-layer graphene[13], but alternatively interpreted in terms of Zener tunnelling. More recently, the same dependence has been reported in twisted bilayer graphene heterostructures, where the SE develops on top of a saturation current[14], with a sign reversal of the Hall effect as an additional signature. Our experiment is motivated by the study of transport in bottom-gated (gate voltage V_g) single-layer graphene field-effect transistors, where pair creation is subject to a finite breakdown field at large doping. Most saliently, our experiment investigates the large bias regime where a giant Klein collimation establishes a quasi-1D transport characterized by a transport gap, and where the SE is accurately fitted by the 1D pair-creation rate with a finite Schwinger bandgap Δ_S. It develops over a ballistic junction of length $\Lambda < 1$ µm set by the gate dielectric thickness (Interpretation of the Schwinger voltage), which builds up at current saturation. This saturation is due to a large drain-source voltage V that reduces the drain-gate voltage $V - V_g$, inducing a suppression of the electronic density n_d at the drain below the channel density. The latter is given by the density at the source n_s (and the chemical potential at the source μ_s), itself set by the gate voltage V_g. This so-called pinchoff generates a peak effect with a large local electric field prone to the ignition of Schwinger-pair creation, which shows up as the breakdown of the giant Klein collimation. As this situation differs from the canonical vacuum breakdown, we distinctively call it the Klein-Schwinger effect (KSE).

Let us detail theoretical prediction for the mesoscopic 1D SE, as sketched in Fig. 1a. Pair creation is monitored by the current generated across the junction upon dissociation in the large electric field. Starting from the 1D Schwinger rate in equation (1), and taking into account the factor 2 for pair dissociation, as well as spin and valley degeneracies g_s and g_v, the pair current I_S and differential conductance G_S can be written as:

$$w_{1d} = \frac{2e}{h}E\sum_{n=1}^{\infty}\frac{e^{-n\pi\frac{E_S}{E}}}{n} = \frac{2e}{h}E\ln\left(\frac{1}{1-e^{-\pi\frac{E_S}{E}}}\right) \quad (1)$$

$$I_S = 4V\ln\left(\frac{1}{1-e^{-\pi\frac{V_S}{V}}}\right) \times g_sg_v\frac{e^2}{h} \qquad \text{with} \qquad V_S = \Lambda E_S = \Lambda\frac{\Delta_S^2}{e\hbar v_F} \quad (2)$$

$$G_S = 4\left[\frac{\pi\frac{V_S}{V}}{e^{\pi\frac{V_S}{V}}-1} + \ln\left(\frac{1}{1-e^{-\pi\frac{V_S}{V}}}\right)\right] \times g_sg_v\frac{e^2}{h} \quad (3)$$

$$\approx 1.20\left(\frac{V}{0.62V_S} - 1\right) \times g_sg_v\frac{e^2}{h} \qquad (V_C = 0.62V_S \lesssim V \lesssim 2V_S) \quad (4)$$

where V is the total bias and V_S the Schwinger voltage, product of the Schwinger field $E_S = \frac{\Delta_S^2}{e\hbar v_F}$ by the length Λ of the pair-creation domain. The differential conductance (equation 3) possesses an inflection point at $V = 1.22\ V_S$, supporting an affine approximation given by equation (4) and characterized by a critical voltage $V_C = 0.62\ V_S$ and a zero-bias extrapolate $-G_0$ stemming from a quantized pair conductance $G_0/g_sg_v = 2 \times 0.60\ \frac{e^2}{h}$ (per spin and valley), with the prefactor 2 as a tag for pair dissociation. The Schwinger conductance (equation 3) is plotted in Fig. 1b for 1D graphene, where $g_s = g_v = 2$ (solid red line), including the affine approximation (dotted black line for equation (4)) with $G_0 = 0.186$ mS. Also shown in the figure is the conductance $G_S^* = 4g_sg_v\frac{e^2}{h}\left(1 + \pi\frac{V_S}{V}\right)e^{-\pi\frac{V_S}{V}}$ (dash-dotted blue line) calculated with the Schwinger rate (equation 1) truncated to its first $n = 1$ term; the truncated variant deviates from the full Schwinger conductance for $V/V_S \gtrsim 1.5$ and $G_S \gtrsim 0.2$ mS. Comparison of massive 1D and 2D Schwinger conductances, as well as that of three-dimensional Schwinger and the non-relativistic Fowler–Nordheim mechanism, are contrasted as discussed in Supplementary Discussion Section I.

Measurements are performed at room temperature in a series of six hBN-encapsulated single-layer graphene transistors deposited on local backgates, made of graphite for devices GrS1–3 and gold for devices AuS1–3, and equipped with high-transparency edge contacts (Methods and Supplementary Table I). As explained below (Klein collimation junction), high mobilities $\mu \gtrsim 10\ \mathrm{m^2\,V^{-1}\,s^{-1}}$, large dimensions $(L, W) \gtrsim 10$ µm, high doping n_s and small-gate dielectric thicknesses $t_{hBN} \lesssim 100$ nm, are key ingredients for observing the SE. High mobility provides current saturation at low bias $V_{sat} < V_g$, whereas high doping and long channels are needed to reject the Zener channel instability at a large bias $V_Z > V_g$. The SE is visible in the bias window $[V_{sat}, V_Z]$ where Klein collimation is effective, at a Schwinger voltage $V_S \approx V_g$ controlled by the channel doping n_s and dielectric thickness t_{hBN}. Data reported below refer mostly to the representative GrS3 sample, leaving the full sample series description for Supplementary Discussion Section IV.

Klein collimation junction

Prior to discussing the SE in the next section, it is worth understanding the electric field profile it stems from, and the current saturation mechanism. We show in Fig. 2a the high-bias current-voltage (I-V) characteristics of sample GrS3 (Fig. 2 caption), which exhibit prominent current saturation plateaus centred at the $I(V = V_g)$ pinchoff line (dashed black line). The highlighted $V_g = 3$ V trace (thick turquoise line) illustrates the three main transport regimes: (1) the diffusive Drude regime for $V \lesssim V_{sat}$, (2) the Klein collimation saturation regime for $V_{sat} \lesssim V \lesssim V_Z$

https://doi.org/10.1038/s41567-023-01978-9

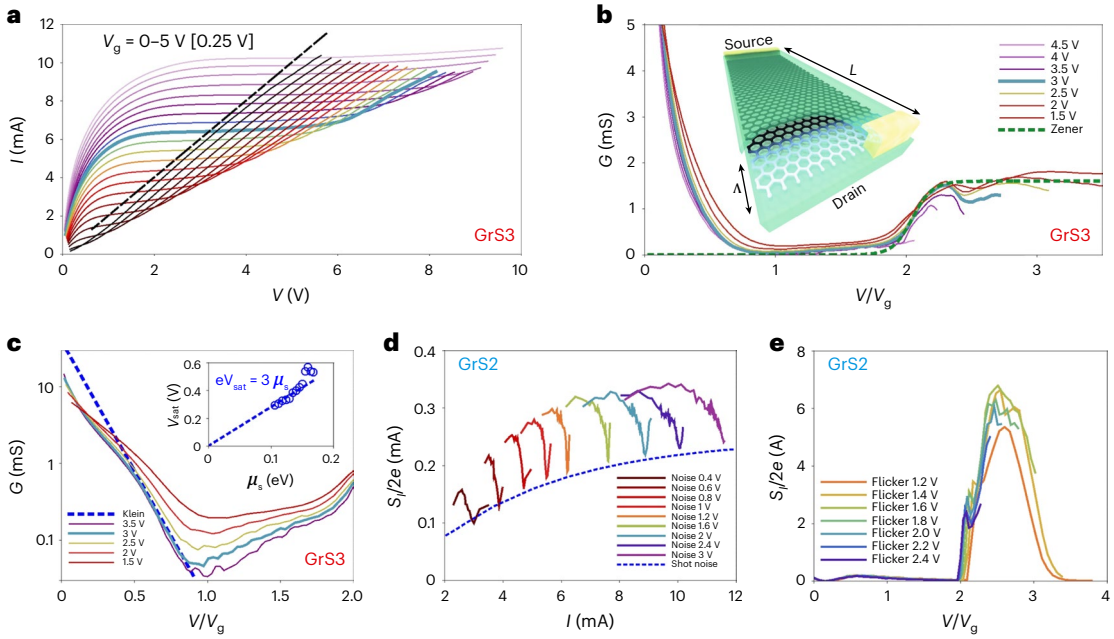

Fig. 2 | Room temperature ballistic pinchoff in sample GrS3 of dimensions $L \times W \times t_{hBN} = 15 \times 10 \times 0.042$ µm, mobility $\mu = 12 m^2 V^{-1} s^{-1}$ (gate capacitance $C_g = 0.67$ mFm^{-2}) and contact resistance $R_c = 120$ Ω. a, Set of current–voltage characteristics after subtraction of contact voltage drop, including the representative $V_g = 3$ V trace (thick turquoise line). The pinchoff regime $V = V_g$ is indicated by the dashed black line. **b**, Differential conductance scaling $G\left[\frac{V}{V_g}\right]$ illustrating the steep decay of saturation conductance below pinchoff, and the sharp onset of Zener conductance at twice the pinchoff voltage. Inset is an artist's view of the supposed carrier density distribution, characterized by a sharp drop over a collimation length Λ at the drain side. **c**, Semilog representation of conductance showing the exponential decay at current saturation, $G = G(0)e^{-\frac{V}{V_{sat}}}$ (dotted blue line), with a doping-dependent saturation voltage $V_{sat} \simeq 3\mu_s/e$ (dashed line in the inset). **d**, High-frequency (1–10 GHz) current noise measured in sample GrS2 at $T = 10$ K as a function of current. The sharp drop at pinchoff maps the vanishing of the thermal noise contribution $S_I = 4G(I)k_BT_e$, where T_e is the hot-electron temperature, according to the differential conductance dip at saturation. The residual noise (dashed blue line) is attributed to shot noise $S_I = 2eIF$ obeying the Fano factor $F \simeq 0.04/\sqrt{1 + (I_{sat}/0.006)^2}$. **e**, Huge low-frequency (0.1–1 MHz) current noise peak at the onset of the Zener instability.

and (3) the Zener regime for $V \gtrsim V_Z$. As discussed in previous works[15,16], the Zener effect corresponds to a field-induced bulk interband Klein tunnelling and is characterized by a doping- and bias-independent Zener channel conductivity ($\sigma_Z \approx 1$ mS). It is subject to Pauli blockade leading up to a finite threshold voltage $V_Z = LE_Z$ with a critical Zener field $E_Z \propto \mu_s^2 \propto n_s$ (ref. [16]). Consequently the Zener voltage $V_Z \propto LV_g$ of long transistors is rejected well above V_g. This important feature characterizes our device series (Supplementary Discussion Section IV), which differs from conventional devices[17,18] where lower mobility and shorter channel lengths substitute saturation plateaus by a crossover between the Drude and Zener ohmic regimes.

In Supplementary Discussion Section VI we compare the pinchoff-induced exponential current saturation observed in the present V_g = Constant biasing mode, with the current obtained in the pinchoff-free drain-doping-compensated mode[15]. We also provide a simple 1D model of the electrostatic potential distribution in the channel to estimate the respective channel and collimation junction voltage drops in the pinchoff regime, thereby establishing the existence of a Klein collimation junction. Klein collimation is the semimetal variant of the pinchoff junction of metal oxide semiconductor field-effect transistors[19]. The exponential saturation is reminiscent of the collimation effect of gate-defined long p–n junctions[20], characterized by a transmission $T(k_y) \approx \exp(-\pi\hbar v_F k_y^2/eE_x)$ where $k_y = k_F \sin\theta$ is the transverse projection of the Fermi wave vector, θ is the angle of incidence and $E_x = 2\mu_s/\Lambda$ is the built-in in-plane electric field[20–22]. This p–n junction model, where electrons with a finite transverse momentum acquire a 1D massive Dirac fermion character with a gap $2\hbar v_F k_y$, provides a natural framework for the bias-induced giant Klein collimation reported here. In contrast to the p–n junction case, Klein collimation entails large $E_x \simeq V/\Lambda$ and $\hbar v_F k_y = eV \sin\theta_{sat}$, leading to an exponentially vanishing transmission $T(V) \approx \exp(-\pi V \frac{e\Lambda}{\hbar v_F} \sin^2\theta_{sat})$. This giant Klein collimation effect turns an incident 2D electron gas into a 1D transmitted beam, leading to an emergent 1D transport regime of relativistic electrons at a velocity v_F.

Current saturation is best characterized by the differential conductance $G = \partial I/\partial V$, whose scaling properties as a function of V/V_g are shown in Fig. 2b. The high-bias Zener regime corresponds to a doping-independent step-like increase to the Zener conductance $G_Z \simeq 1.5$ mS at $V_Z \simeq 1.8\,V_g$. The saturation regime of interest in this work is characterized by a vanishing conductance in the $[V_{sat}, V_Z]$ window. Figure 2c is a semilog plot showing the exponential decay of the saturation conductance above the saturation voltage V_{sat}. It is exemplified by the dashed blue-line fit of the representative $V_g = 3$ V data. This exponential decay is observed over a broad doping range, and characterized by a doping-dependent saturation voltage V_{sat} according to the fitting law $G = G(0)e^{-V/V_{sat}}$. The inset shows the Fermi energy dependence of V_{sat}, which obeys a linear law $V_{sat} \simeq 3\mu_s/e$, implying that tunnelling-conductance suppression at pinchoff, $G(V_g \propto \mu_s^2) \propto e^{-\mu_s/\text{Constant}}$, increases with doping. This property is consistently observed in the full sample series (Supplementary Table 1) where $eV_{sat}/\mu_s = 2.5$–5. In the above p–n junction model, the saturation voltage $V_{sat} = \hbar v_F/\pi e\Lambda \sin^2\theta_{sat}$ is related to the collimation angle θ_{sat}.

An additional signature of the existence of a Klein junction is found in the transistor shot noise in Fig. 2d. Shot noise $S_I = 2eI\mathcal{F}$, where $\mathcal{F} \lesssim 1$ is the Fano factor, is deduced from the microwave current noise S_I, which adds to the thermal noise $S_I = 4G(I)k_BT_e$, where k_B is the Boltzmann constant and T_e is the electronic temperature. Here we take advantage

https://doi.org/10.1038/s41567-023-01978-9

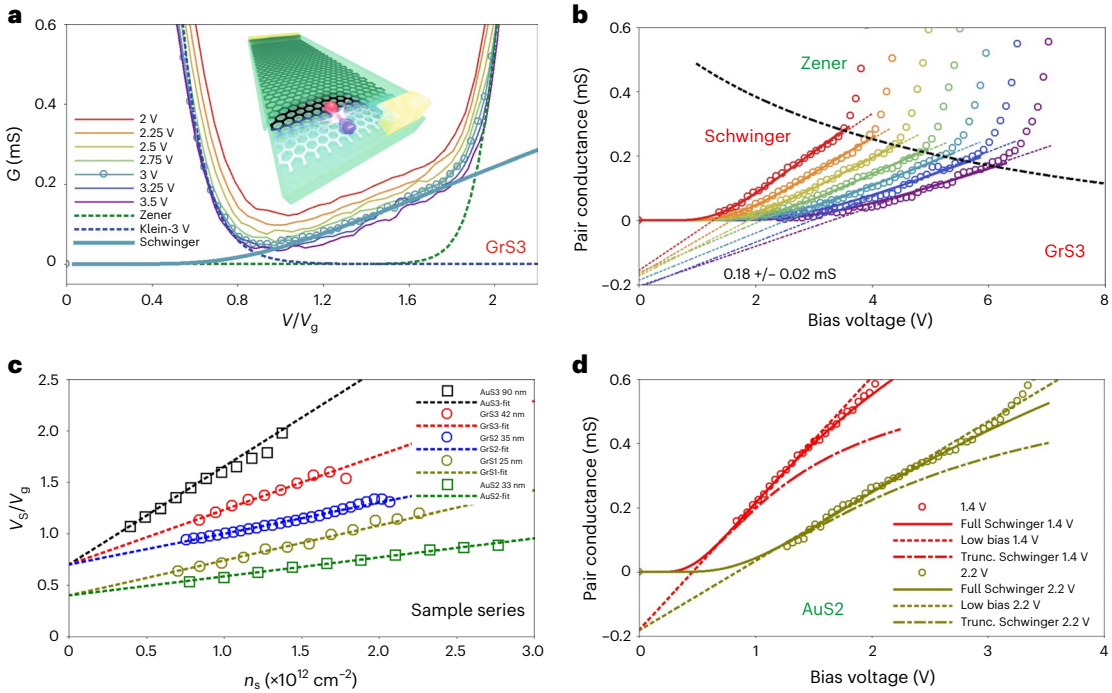

Fig. 3 | KSE in long ballistic transistors. a, Blow-up of GrS3 conductance in Fig. 2b. The fully developed gap at large doping (dashed blue and green lines of the $V_g = 3$ V data) unveils the Schwinger-pair contribution (thick turquoise line) corresponding to $V_S \simeq 1.4\ V_g$. Inset: Artist's view of the Klein-Schwinger mechanism. At lower doping, where the Schwinger contribution is embedded in a finite Klein contribution, the pair contribution is extracted from the single-particle tunnelling contribution by a three-parameter fit of conductance data according to the law $G(V) = G_S(V/V_S) + G(0)e^{-V/V_{sat}}$. **b**, The pair contribution $G(V) - G(0)e^{-V/V_{sat}}$ (same colour code as in **a**), reveals the affine approximation scaling of the Schwinger conductance (equation 4) with $G_0 \simeq 0.18 \pm 0.02$ mS and $V_S = 0.7V_g + 0.15V_g^2$. The Zener regime is signalled by a sharp increase of pair conductance above the Schwinger–Zener boundary (dotted black line) set by $G_S(V = V_Z = 1.9\ V_g)$. **c**, Linear increase of the $V_S/V_g(n_s)$ ratio with doping observed in the full transistor series (Supplementary Fig. 7) where Schwinger-pair conductance scaling is reported with consistent values of G_0. The slope increases with dielectric thickness (main text). The V_S/V_g ratio is minimized in sample AuS2 ($L \times W \times t_{hBN} = 10.5 \times 15 \times 0.035$ μm) and maximized in sample AuS3 ($L \times W \times t_{hBN} = 11.1 \times 11.4 \times 0.090$ μm). **d**, Broad-range ($V/V_S \lesssim 4$) Schwinger conductance at low doping in AuS2 where $V_S/V_g \simeq 0.5$ showing the quantitative agreement with equation (3) (solid lines) that deviates from the affine approximation (equation 4) (dotted lines), and from the truncated approximation G_S^* (dash-dotted lines).

of the conductance suppression at saturation, with $G(I \simeq I_{sat}) \to 0$ corresponding to the noise dips at the saturation current I_{sat} in Fig. 2d, to extract the junction Fano factor $\mathcal{F}(I_{sat}) \lesssim 0.04$(Supplementary Discussion Section III). The presence of a shot noise, and the tiny value of the Fano factor, are strong indications of the presence of a ballistic junction[23]. Finally, the Zener threshold is reached upon increasing further the bias voltage; it entails an upheaval of the electric field distribution, as the electric field, initially confined over Λ in the Klein collimation regime, penetrates the full channel length L in the ohmic Zener regime. A signature of this collective instability of Klein collimation can be seen in the huge low-frequency current noise observed over the $[V_Z, 1.5\ V_Z]$ range in Fig. 2e.

The exponential current saturation, the presence of shot noise and the Zener electric field instability are three independent signatures of the giant Klein collimation effect and its collective instability towards a bulk Zener effect. The Klein collimation and its associated high-field region will act as a seed for the SE demonstrated below.

Evidence of a universal 1D Schwinger conductance

To highlight the small Schwinger-pair contribution in transport, we magnify in Fig. 3a the conductance-scaling plot of Fig. 2b. We focus first on the $V_g = 3$ V data (turquoise circles), for which the exponential tails of the Klein collimation (dotted blue line) and Zener (dotted green line) contributions are fully suppressed in a bias window $[1.1\ V_g, 1.7\ V_g]$. In this window, the measured conductance is solely governed by the Schwinger contribution, as evidenced by the fit of $V_g = 3$ V data with equation (3) taking $V_S = 1.4\ V_g$ (thick turquoise line). The SE is also visible at lower doping, albeit partially obscured by a residual Klein tunnelling contribution. To extract the Schwinger contribution at arbitrary doping, we rely on the de-embedding of the Klein tunnelling contribution using a three-parameter fit $G = G_S(V/V_S) + G(0)e^{-V/V_{sat}}$ performed in the relevant range $[V_{sat}, V_Z]$. The resulting pair conductance G_S is displayed in Fig. 3b. It highlights the sharp transition (dotted black line) separating the Schwinger and Zener regimes, and reveals the Schwinger conductance fan-like scaling predicted by the affine approximation (equation 4) for a doping-dependent V_S. Remarkably, the linear zero-bias extrapolate is a constant $G_0 \simeq 0.18 \pm 0.02$ mS, which is very close to the universal quantization $G_0 = 1.20\frac{4e^2}{h} = 0.186$ mS for the 1D SE in graphene. The same procedure has been applied to the full sample series in Supplementary Figs. 6 and 7, which shows similar scaling with consistent values of G_0. This observation of a robust conductance quantization, in quantitative agreement with 1D Schwinger theory, is a parameter-free demonstration of the relevance of 1D SE, and of its ubiquity in high-mobility graphene transistors, which constitutes the main finding of our work.

Interpretation of the Schwinger voltage

Going one step further, we analyse the dependence of the Schwinger voltage $V_S(n_s, t_{hBN})$ on doping n_s and hBN thickness t_{hBN}, extracted from theoretical fits of pair-conductance data with (equation 3). We assume that $V_S(n_s, t_{hBN}) = E_S(n_s)\Lambda(n_s, t_{hBN})$ with $E_S = \Delta_S^2(n_s)/e\hbar v_F$ for a Schwinger gap Δ_S set by a collimation gap $2\hbar v_F k_S$ at finite transverse momentum k_S. In high-energy physics, the Schwinger threshold for

electron–positron creation in a vacuum (the absence of any other particles before pair creation) is set by a true spectral gap $2mc^2$. In condensed matter, the threshold for electron–hole creation can also be associated to a Pauli blocking effect related to the presence of other electrons filling graphene bands before pair creation. For the KSE, we assume heuristically that this threshold energy is set by $2\hbar v_F k_s$, where k_s is a typical transverse momentum for the fully populated Klein transmitted electrons. In the absence of a fully fledged theory, and for the purpose of estimating the Klein collimation length $\Lambda(n_s, t_{hBN})$, we use the Ansatz $\Delta_S \simeq \mu_s$.

We plot in Fig. 3c the ratio $V_S/V_g(n_s)$ for the full device series. We observe a linear doping dependence with a slope that increases with gate dielectric thickness t_{hBN} = 25–90 nm. As detailed in the Supplementary Discussion Section V, these dependencies can be explained by $\Lambda(n_s, t_{hBN})$, according to the law $\frac{\Lambda}{t_{hBN}}\frac{\Delta_S^2}{\mu_s^2} = 4\alpha_g\frac{V_S}{V_g}$, where $\alpha_g = \frac{e^2}{4\pi\epsilon_{hBN}\varepsilon_0\hbar v_F} = 0.70$ (with ϵ_{hBN} = 3.1 at high field[12]) is the graphene fine structure constant. Assuming that $\Delta_S \simeq \mu_s$, we can cast the measured $\frac{V_S}{V_g}(t_{hBN}, n_s)$ into the t_{hBN} power expansion $\Lambda \simeq at_{hBN} + \xi n_s t_{hBN}^2$, where a = 1–2 is a geometrical factor depending on the details of the contact gate arrangements, and $\xi \simeq 4$ nm is a microscopic interaction length (ξ is the typical interaction radius per electron (for $n_s t_{hBN}^2 = 1$) fitting in a junction length $\Lambda \approx t_{hBN}$), quantifying the doping-induced dilation of the junction length. This Coulomb repulsion effect enhances V_S, favouring the visibility of the KSE at large doping (GrS3 data in Fig. 3c), up to the limit where its onset exceeds V_Z so that the SE becomes masked by the Zener instability (AuS3 data in Fig. 3c). The latter case prevails in thick-hBN samples, giving rise to extremely flat current saturation plateaus (Supplementary Fig. 4f). Conversely, the small $V_S/V_g \simeq 0.5$ ratio of thin-hBN samples (AuS2 data in Fig. 3c), allows for investigating conductance over an extended bias range $V/V_S \lesssim 4$. The doping and hBN-thickness dependencies of the ratio V_S/V_g, which contrast with the constant V_Z/V_g, support our interpretation of the SE as the intrinsic breakdown mechanism of Klein collimation, rather than a precursor of the extrinsic (length-dependent) collective Zener instability.

We conclude our experimental report by analysing the extended Schwinger conductance regime in the AuS2 data, which are plotted in Fig. 3d. The accessible experimental range of Schwinger conductance ($G_S \lesssim 0.6$ mS) exceeds the validity domain ($G_S \lesssim 0.2$ mS) of the affine approximation (4), unveiling the sublinearities involved in equation (3) (solid lines). Experimental data are in excellent agreement with the full non-perturbative 1D Schwinger prediction, substantially deviating from the affine approximation (dotted lines), and strongly deviating from the truncated-rate 1D Schwinger conductance G_S^* (dash-dotted lines). This observation constitutes complementary evidence of the relevance of the Schwinger theory[3].

The demonstration of the SE in an effective field theoretical 1 + 1D system is, to our knowledge, the first of its kind and a confirmation of a crucial prediction of quantum electrodynamic field theory. It fulfils the promise of using graphene to emulate quantum electrodynamics[24], specifically here in its strong field sector. The use of condensed matter analogues has already proven fruitful in cosmology[25], in particular with the observation of vortex formation in neutron-irradiated superfluid He-3 as an analogue of cosmological defect formation[26], or that of the analogue of black hole Hawking radiation[27], as well as in the understanding of energy renormalization via Lorentz boosts[28].

Our experiment shows the ability of giant Klein collimation to generate large local electric fields. This opens a way for exploration of the SE in different systems, like the massive Dirac fermions in bilayer graphene[11], or the massless fermions in three-dimensional Weyl or Dirac semimetals[29]. In this respect, theoretical challenges remain concerning the modelling of strongly out-of-equilibrium collimation and the emergence of the Schwinger gap. Our experiment also shows that prominent current saturations, with large saturation velocities, can be obtained in gapless graphene. On the application side, the understanding of the Klein-Schwinger mechanism turns out to be the key for the optimization of large voltage gain $A = \partial V/\partial V_g = G_m/G$ (with G_m the transconductance, see Supplementary Fig. 2) in high-mobility graphene transistors, which is tunable from $A \approx 10$ in thin-hBN AuS2 to $A \approx 100$ in thick-hBN AuS3 according to the V_S/V_g ratio (Supplementary Table 1). Our work thus describes the implementation of a fully relativistic Klein-Schwinger field-effect transistor showing large saturation currents and voltage gain.

Finally, one may attempt to go deeper in the condensed matter analogy of quantum electrodynamics by investigating other manifestations of the SE, like the full counting statistics of pair creation, or the vacuum polarization[3] that is a precursor of pair creation. This raises the question of the dynamics of Schwinger-pair creation, which is an open field that can be investigated by dynamical transport and electromagnetic radiation spectroscopy.

Online content

Any methods, additional references, Nature Portfolio reporting summaries, source data, extended data, supplementary information, acknowledgements, peer review information, details of author contributions and competing interests, and statements of data and code availability are available at https://doi.org/10.1038/s41567-023-01978-9.

References

1. Sauter, F. Uber das Verhalten eines Elektrons im homogenen elektrischen Feld nach der relativistischen Theorie Diracs. *Z. Phys.* **69**, 742–764 (1931).
2. Heisenberg, W. & Euler, H. Consequences of Dirac's theory of positrons. *Z. Phys.* **98**, 714–732 (1936).
3. Schwinger, J. S. On gauge invariance and vacuum polarization. *Phys. Rev.* **82**, 664 (1951).
4. Itzykson, C. & Zuber, J. B. *Quantum Field Theory* (McGraw-Hill, 2006).
5. Schutzhold, R., Gies, H. & Dunne, G. Dynamically assisted Schwinger mechanism. *Phys. Rev. Lett.* **101**, 130404 (2008).
6. Gavrilov, S. P. & Gitman, D. M. Vacuum instability in external fields. *Phys. Rev. D.* **53**, 7162 (1996).
7. Schutzhold, R. Recreating fundamental effects in the laboratory? *Adv. Sci. Lett.* **2**, 121 (2009).
8. Shytov, A., Rudner, M., Gu, N., Katsnelson, M. & Levitov, L. Atomic collapse, Lorentz boosts, Klein scattering, and other quantum-relativistic phenomena in graphene. *Solid State Commun.* **149**, 1087–1093 (2009).
9. Dora, B. & Moessner, R. Non-linear electric transport in graphene: quantum quench dynamics and the Schwinger mechanism. *Phys. Rev. B* **81**, 165431 (2010).
10. Gavrilov, S. P., Gitman, D. M. & Yokomizo, N. Dirac fermions in strong electric field and quantum transport in graphene. *Phys. Rev. D.* **86**, 125022 (2012).
11. Katsnelson, M. I. & Volovik, G. E. Quantum electrodynamics with anisotropic scaling: Heisenberg–Euler action and Schwinger pair production in the bilayer graphene. *JETP Lett.* **95**, 411–415 (2012).
12. Pierret, A. et al. Dielectric permittivity, conductivity and breakdown field of hexagonal boron nitride. *Mater. Res. Express* **9**, 065901 (2022).
13. Vandecasteele, N., Barreiro, A., Lazzeri, M., Bachtold, A. & Mauri, F. Current-voltage characteristics of graphene devices: interplay between Zener–Klein tunneling and defects. *Phys. Rev. B.* **82**, 045416 (2010).
14. Berdyugin, A. I. et al. Out-of-equilibrium criticalities in graphene superlattices. *Science* **375**, 430–433 (2022).
15. Yang, W. et al. A graphene Zener–Klein transistor cooled by a hyperbolic substrate. *Nat. Nanotechnol.* **13**, 47–52 (2018).

16. Baudin, E., Voisin, C. & Plaçais, B. Hyperbolic phonon polariton electroluminescence as an electronic cooling pathway. *Adv. Funct. Mater.* **30**, 1904783 (2020).
17. Meric, I. et al. Current saturation in zero-bandgap, top-gated graphene field-effect transistors. *Nat. Nanotechnol.* **3**, 654–659 (2008).
18. Wilmart, Q. et al. High-frequency limits of graphene field-effect transistors with velocity saturation. *Appl. Sci.* **10**, 446 (2020).
19. Sze, S. M. & Ng, K. *Physics of Semiconductor Devices* 3rd edn, Ch. 7, p. 389 (Wiley, 2007).
20. Cheianov, V. V. & Falko, V. I. Selective transmission of Dirac electrons and ballistic magnetoresistance of n–p junctions in graphene. *Phys. Rev. B* **74**, 041403(R) (2006).
21. Cayssol, J., Huard, B. & Goldhaber-Gordon, D. Contact resistance and shot noise in graphene transistors. *Phys. Rev. B* **79**, 075428 (2009).
22. Sonin, E. B. Effect of Klein tunneling on conductance and shot noise in ballistic graphene. *Phys. Rev. B* **79**, 195438 (2009).
23. Danneau, R. et al. Shot noise in ballistic graphene. *Phys. Rev. Lett.* **100**, 196802 (2008).
24. Novoselov, K. S. Nobel lecture. Graphene: materials in the flatland. *Rev. Mod. Phys.* **83**, 837 (2011).
25. Zurek, W. H. Cosmological experiments in condensed matter systems. *Phys. Rep.* **276**, 177–221 (1996).
26. Ruutu, V. M. et al. Vortex formation in neutron-irradiated superfluid 3He as an analogue of cosmological defect formation. *Nature* **382**, 334–336 (1996).
27. de Nova, J. R. M., Golubkov, K., Kolobov, K. V. I. & Steinhauer, J. Observation of thermal Hawking radiation and its temperature in an analogue black hole. *Nature* **569**, 688–691 (2019).
28. Wyzula, J. et al. Lorentz-boost-driven magneto-optics of the nodal-line semimetal $NbAs_2$. *Adv. Sci.* **9**, 2105720 (2022).
29. Katsnelson, M. I. & Volovik, G. E. Topological matter: graphene and superfluid He. *J. Low Temp. Phys.* **175**, 655–666 (2014).

Methods

Fabrication of ballistic graphene transistors

The hexagonal boron nitride encapsulated graphene heterostructures are fabricated with the standard pick-up and stamping technique, using a polydimethylsiloxane/ polypropylenecarbonate stamp[30]. The gate is first fabricated on a high-resistivity Si substrate covered by 285 nm SiO_2. The gate electrode is either a thin exfoliated graphite flake (thickness $\lesssim$ 15 nm) or a prepatterned gold pad (thickness 70 nm) designed by laser lithography and Cr/Au metallization. Deposition of the heterostructure on the backgate is followed by acetone cleaning of the stamp residues, Raman spatial mapping and atomic force microscopy characterization of the stack. Graphene edge contacts are then defined by means of laser lithography and reactive ion etching, securing low contact resistance $\lesssim 1\,k\Omega\,\mu m$. Finally, metallic contacts to the graphene channel are designed with a Cr/Au Joule evaporation that also embeds the transistor in a coplanar waveguide geometry suited for cryogenic probe station microwave and noise characterization. The large transistor dimensions $L, W \gtrsim 10\,\mu m$ secure moderate channel electric field $E \approx V/L \lesssim 10^6\,V\,m^{-1}$ up to the metal oxide semiconductor field-effect transistor pinchoff at $V = V_g$, while their high mobility $\mu \gtrsim 6\,m^2V^{-1}s^{-1}$ at room temperature, and $\mu \gtrsim 35\,m^2V^{-1}s^{-1}$ at 10 K, secures ballistic transport in the channel.

Radio-frequency transport and noise measurement

Characterization of the ballistic graphene transistors is performed in a cryogenic probe station adapted to radio-frequency measurements up to 67 GHz. The d.c. measurements are performed using a Keithley 2612 voltage source to apply gate and bias. Noise measurements are enabled by the use of a Tektronix DPO71604C ultrafast oscilloscope for measurements up to 16 GHz. The high-frequency signal coming from the device is amplified by a CITCRYO1-12D Caltech low noise amplifier in the 1–10 GHz band, whose noise and gain have been calibrated against the thermal noise of a 50 Ω calibration resistance measured at various temperatures between 10 K and 300 K in the probe station. For low-frequency noise measurements in the 0.1–1 MHz band, an NF Corporation amplifier (SA-220F5) is used.

Data availability

Data are available at https://doi.org/10.5281/zenodo.7104630. Source data are provided with this paper.

Reference

30. Yankowitz, M., Ma, Q., Jarillo-Herrero, P. & LeRoy, B. J. Van der Waals heterostructures combining graphene and hexagonal boron nitride. *Nat. Rev. Phys.* **1**, 112–125 (2019).

Acknowledgements

The research leading to these results has received partial funding from the European Union Horizon 2020 research and innovation programme under Grant Agreement No. 881603 Graphene Core 3 (D.M., M.R., E. Baudin, B.P.). P.V. and J.C. were supported by the "LIGHT S&T Graduate Program" (PIA3 Investment for the Future Program, ANR-17-EURE-0027) and GPR LIGHT.

Author contributions

A.S., E. Baudin and B.P. conceived the experiment. A.S. conducted device fabrication and measurements, under the guidance of D.M. and M.R. in the early developments. T.T. and K.W. provided the hBN crystals. P.V., J.C., M.O.G., E. Baudin, J.T. and B.P. developed the models and theoretical interpretations. A.S., D.M., C.V., J.M.B., E. Bocquillon, G.F., C.V., E. Baudin and B.P. participated in the data analysis. A.S., E. Baudin and B.P. wrote the manuscript with contributions from the coauthors.

Competing interests

The authors declare no competing interests.

Additional information

Supplementary information The online version contains supplementary material available at https://doi.org/10.1038/s41567-023-01978-9.

Correspondence and requests for materials should be addressed to A. Schmitt, E. Baudin or B. Plaçais.

Peer review information *Nature Physics* thanks Ethan Minot and the other, anonymous, reviewer(s) for their contribution to the peer review of this work.